Calibration of two-dimensional floodplain modeling in the central Atchafalaya Basin Floodway System using SAR interferometry

Hahn Chul Jung,[1] Michael Jasinski,[1] Jin-Woo Kim,[2] C. K. Shum,[2] Paul Bates,[3] Jeffrey Neal,[3] Hyongki Lee,[4] and Doug Alsdorf[2]

Received 3 February 2012; revised 21 May 2012; accepted 4 June 2012; published 13 July 2012.

[1] Two-dimensional (2-D) satellite imagery has been increasingly employed to improve prediction of floodplain inundation models. However, most focus has been on validation of inundation extent, with little attention on the spatial variations of water elevation and slope. The availability of high resolution Interferometric Synthetic Aperture Radar (InSAR) imagery offers unprecedented opportunity for quantitative validation of surface water heights and slopes derived from 2D hydrodynamic models. In this study, the LISFLOOD-ACC hydrodynamic model is applied to the central Atchafalaya Basin Floodway System, Louisiana, during high flows typical of spring floods in the Mississippi Delta region, for the purpose of demonstrating the utility of InSAR in 2-D floodplain model calibration. Two schemes calibrating Manning's roughness in channels and floodplains are compared. First, the model is calibrated in terms of water elevations at a single in situ gage during a 62-d simulation period from 1 April 2008 to 1 June 2008. Second, the model is calibrated in terms of water elevation changes calculated from ALOS PALSAR 2D imagery acquired on 16 April 2008 and 1 June 2009, an interval of 46 d. The best-fit model shows that the mean absolute error is 5.7 cm/46 d for InSAR water level calibration. Daily storage changes within the ~230-km^2 model area are also calculated to be on the order of 107 m^3 d^{-1} during high water of the modeled period. The favorable comparison between both approaches demonstrates the feasibility of SAR interferometry for 2-D hydrodynamic model calibration and for improved understanding of complex floodplain hydrodynamics.

Citation: Jung, H. C., M. Jasinski, J.-W. Kim, C. K. Shum, P. Bates, J. Neal, H. Lee, and D. Alsdorf (2012), Calibration of two-dimensional floodplain modeling in the central Atchafalaya Basin Floodway System using SAR interferometry, *Water Resour. Res.*, *48*, W07511, doi:10.1029/2012WR011951.

1. Introduction

[2] The Atchafalaya River Basin, a low-lying catchment in southern Louisiana consisting of wetlands and bayous, is the principal distributary of the Mississippi River. Given its high concentration of wetlands and its role as the alternate flow path for Mississippi floodwaters, the Atchafalaya Basin Floodway System (ABFS) possesses an important function in mitigating floods and preserving wetland resources in coastal Louisiana. For example, Mississippi River floodwaters in May 2011, resulting from unusually high precipitation in the watershed, were diverted through the Morganza Spillway into the ABFS to prevent major inundations in populated cities including Baton Rouge and New Orleans [*U.S. Army Corps of Engineers (USACE)*, 2011]. Also, flood damage caused by Hurricane Katrina in August 2005 and Hurricane Rita in September 2005, although significant, was mitigated by flooding into the Atchafalaya Basin [*Lake Pontchartrain Basin Foundation (LPBF)*, 2008; *Knabb et al.*, 2006, 2007]. Flood management has been enabled through the construction of levees, bank protection, and spillways along the Lower Mississippi River, the Atchafalaya, and their tributaries.

[3] Although the man-made levees and river diversions abate flood damage, they also disrupt the natural floodplain environment. Of principal concern is the reduction by more than 50% in the historically large sediment loads deposited within the Lower Mississippi River delta [*LPBF*, 2010], which is a major factor in the land loss in southeastern Louisiana [*Meade*, 1995]. Coastal Louisiana has undergone a net change in land area of about –4877 km^2 from 1932 to 2010 and annual wetland loss has been estimated 42.92 km^2 from 1985 to 2010 [*Couvillion et al.*, 2011]. Comprehensive flood control and wetland loss studies on coastal Louisiana including the ABFS have been initiated to further the understanding of its important role [*U.S. Environmental Protection Agency (USEPA)*, 1987].

[1]Hydrological Sciences Laboratory, NASA Goddard Space Flight Center, Greenbelt, Maryland, USA.
[2]Division of Geodetic Science, School of Earth Sciences, Ohio State University, Columbus, Ohio, USA.
[3]School of Geographical Sciences, University of Bristol, Bristol, UK.
[4]Department of Civil and Environmental Engineering, University of Houston, Houston, Texas, USA.

Corresponding author: H. C. Jung, Hydrological Sciences Laboratory, NASA Goddard Space Flight Center, Bldg. 33, Greenbelt Rd., Greenbelt, MD 20771, USA. (hahnchul.jung@nasa.gov)

0043-1397/12/2012WR011951

[4] Despite its importance to flood control, knowledge of the Atchafalaya Basin's floodplain dynamics remains poor. This is primarily due to a lack of in situ gauge measurements in the floodplain. Most operational gauges are located along main river channels and bayous for practical and economic reasons [*Allen et al.*, 2008; *Kim et al.*, 2009]. Thus, despite long historical data records for the channels, there are insufficient in situ data for detailed 2-D floodplain model calibration [*Allen et al.*, 2008]. This is because water flow across wetlands is more complex than channel routing [*Alsdorf et al.*, 2007; *Jung et al.*, 2010] as flow paths and water sources are not constant in space and time, but rather vary with floodwater elevations.

[5] Advances in remote sensing hydrology, particularly over the past 10 yr and even more recently, have demonstrated that hydraulic variables can be measured reliably from satellites [*Alsdorf et al.*, 2007]. Therefore, 2-D flood modeling combined with emerging remotely sensed data would greatly facilitate the investigation of the temporal and spatial flooding patterns and further the understanding of the linkage between channels and floodplains.

[6] The first popular approach to fluvial hydraulics modeling was one-dimensional finite difference solutions of the full St. Venant equations along the river reach [e.g., *Fread*, 1985; *Samuels*, 1990; *Ervine and MacLeod*, 1999] since the l-D model design and implementation are simple and computationally efficient (e.g., MIKE11 [*DHI Water and Environment*, 2001], ISIS [*ISIS FLOW*, 2001], FLUCOMP [*Samuels and Gray*, 1982], and HEC-RAS [*USACE*, 2001]). However, when applied to floodplain flows, the l-D model cannot simulate lateral diffusion of the flood wave. This is because floodplain topography in those models is discretized as cross-sections rather than as a surface and flow depends on the location and orientation of finite cross-section measurements [*Hunter et al.*, 2008].

[7] The growing availability of spaceborne data and advances in computing resources have enhanced the opportunities to estimate flood inundation extent, floodplain water elevation, and to model floodplain hydrodynamics [*Hess et al.*, 1995; *Smith*, 1997; *Alsdorf et al.*, 2000; *Bates et al.*, 1992]. For instance, high-resolution light detection and ranging (LiDAR) elevation maps enable modelers to represent an improved spatial resolution of channel and floodplain hydraulics that are consistent with known processes [*Bates et al.*, 2005]. Repeat-pass synthetic aperture radar (SAR) interferometry has recently been employed to estimate water level changes with time [*Alsdorf et al.*, 2000] and, when combined with modeling, storage changes [*Alsdorf*, 2003] and flow hydraulics [*Alsdorf et al.*, 2005]. Satellite SAR interferometry has been utilized to characterize complex fluvial environments [*Kim et al.*, 2009; *Lu et al.*, 2009; *Lee et al.*, 2009; *Jung et al.*, 2010]. Because radar pulse interactions with inundated vegetation typically follow a double-bounce travel path that returns energy to the antenna, flooded woody vegetation in this study area allows SAR interferometric coherence to be maintained and makes it possible to provide water elevation changes [*Lu et al.*, 2005; *Lu and Kwoun*, 2008; *Jung and Alsdorf*, 2010].

[8] Two-dimensional models in conjunction with suitably resolved and accurate digital elevation models (DEMs) of the channel and floodplain, and with suitable inflow and outflow boundary conditions, allow the water depth and depth-averaged velocity to be computed [*Bates et al.*, 2005]. Many 2-D hydraulic modeling approaches discretized the floodplain as a high-resolution regular grid (e.g., TUFLOW [*Syme*, 1991], DIVAST [*Falconer*, 1986], TRENT [*Villanueva and Wright*, 2006], JFLOW [*Bradbrook et al.*, 2004], and LISFLOOD-FP [*Bates and De Roo*, 2000]). Structured-grid 2-D flood inundation modeling has been widely used to predict floodplain inundation since first proposed by *Zanobetti et al.* [1970].

[9] The work presented here complements previous investigations of Atchafalaya River hydrology. For example, previous modeling studies have focused on the spatial and volumetric changes of water, sediment, and salinity in the delta and coastal regions located at outlets of the ABFS [e.g., *Donnell et al.*, 1991; *Donnell and Letter*, 1992; *Wang et al.*, 1995; *Vaughn et al.*, 1996], although they did not implement 2-D modeling to compute floodplain water variations. Other studies demonstrated the feasibility to measure floodplain water elevation changes with in situ measurements in combination with InSAR altimetry [*Lu et al.*, 2005; *Lu and Kwoun*, 2008; *Lee et al.*, 2009; *Kim et al.*, 2009]. Other studies using visible and infrared Landsat imagery have delineated land-water classification within the ABFS [*Allen et al.*, 2008].

2. Study Objective

[10] The calibration of 2-D floodplain models is usually limited by few or no water level gauges in the floodplain, making it difficult to validate detailed spatial variations in inundation. While remote sensing methods have been utilized to evaluate the accuracy of modeled flooding extent [e.g., *Wilson et al.*, 2007; *Di Baldassarre et al.*, 2009], few modeling studies have implemented current satellite SAR interferometric phase measurements of water elevation changes because the processing of SAR interferometry for generating hydrologic products is not straightforward.

[11] The goal of the present study is to investigate to what extent SAR interferometry can be used to improve model calibration. Specifically, the 2-D LISFLOOD-ACC model [*Bates et al.*, 2010] is applied to the central ABFS together with repeat-pass interferometry from the Advanced Land Observing Satellite (ALOS) Phased Array type L-band Synthetic Aperture Radar (PALSAR). LISFLOOD represents l-D diffusive channel flow and 2-D simplified shallow water floodplain flow [*Bates et al.*, 2010]. Satellite InSAR data, namely PALSAR, are used to derive flood levels changes and water surface slopes at times of SAR data acquisitions.

[12] LISFLOOD is calibrated using two different approaches, both focusing primarily on Manning's equation. First, a traditional approach using gauge measurements is employed. Second, the same model is calibrated using the 2-D water level and slope data extracted from two PALSAR interferometric images, acquired 46 d apart. The results of both approaches are compared and the merits and disadvantages of each are discussed. The PALSAR-derived floodplain water elevation change is also used to generate a time series of water storage changes in the model area.

[13] This study offers new insights in 2-D hydrodynamic modeling, particularly in floodplain environments. The complexity of floodwaters has not been well captured in

previous modeling studies because floodwaters move laterally across wetlands and this movement is not bounded like that of a typical channel flow. This study of 2-D hydrodynamic modeling and the implementation of SAR interferometry for model calibration aims to improve our understanding of the Atchafalaya floodplain dynamics and provide an opportunity to investigate the impacts of flood hazard in the coastal Louisiana regions.

3. Study Area

[14] The ABFS, a large low-lying wetland bounded on the east and west by levees, is characterized by 2500 km^2 of the nation's most significant extents of bottomland hardwoods, swamps, bayous, and backwater lakes [*Allen et al.*, 2008]. As a major distributary of the Mississippi, it annually receives nearly 30% of the Mississippi River water which flows south through the floodplain to the Gulf of Mexico along ~225 km of river reach [*Louisiana Department of Natural Resources (LDNR)*, 2010; *Kim et al.*, 2009]. In the spring, the basin receives water carrying high loads of sediment and nutrients [*Allen et al.*, 2008]. As a consequence of frequent flooding, the basin is a sparsely populated area holding a rich abundance and diversity of vegetation species. Figure 1 shows the study area including rivers, levees, gauges, the ALOS PALSAR swath, and model domain. The U.S. Geological Survey (USGS) National Wetlands Research Center and the U.S. Army Corps of Engineers (USACE) provide available gauge stations in the study area.

[15] The USACE has identified 13 sub-basins or water management units (WMU) because of morphological diversity within the basin [*USACE*, 1982]. Figure 2 shows the WMUs outlined in gray. Because of the unique character of each WMU, fluctuating river levels can result in very different patterns of water distribution among them. For the current study, LISFLOOD was applied specifically to the Buffalo Cove WMU, an area of 230 km^2 in the central ABFS (see Figures 1, 2). The WMU is characterized by a swamp forest with paths of slowly moving water or bayous. This WMU was selected because of the proximity of in situ and satellite measurements, and because its upstream, downstream, and lateral boundary conditions are well defined. Buffalo Cove is surrounded by the main channel on the east and a levee on the west (Figure 2) with water level gauge stations at Myette Points (C3) in the channel and Buffalo Cove (B1) in the bayou, shown in Figure 3.

4. Methods and Data

4.1. Hydrodynamic Model

[16] An inertial and parallel version of LISFLOOD-FP hydrodynamic model, or LISFLOOD-ACC [*Bates and De Roo*, 2000; *Bates et al.*, 2010], was applied to the Buffalo Cove WMU. LISFLOOD-ACC is a simplified shallow water model that allows the use of a larger stable time step than previous LISFLOOD-FP variants, and hence quicker run times in addition to a better representation of the flow physics [*Bates et al.*, 2010; *Neal et al.*, 2011]. Channel

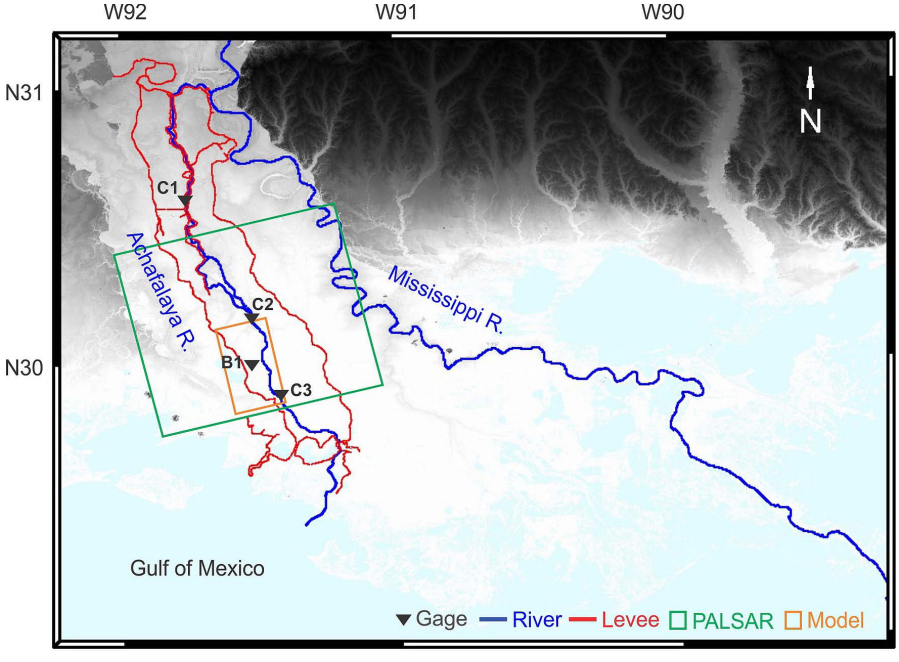

Figure 1. LiDAR map over the study area. The ABFS is bounded on the east and west sides by levees in southern Louisiana. The upstream main channel in the basin diverts the Lower Mississippi River and flows out to the Gulf of Mexico. The orange rectangular box represents the model study area and the green diagonal box indicates the ALOS PALSAR swath. The Atchafalaya River and Mississippi River are represented by blue lines. Levees and gauges are marked with red lines and inverted black triangles. Gage stations are located at (C1) Krotz Springs and (C3) Myette Point along the main channel and at (B1) Buffalo Cove in the bayou, whereas C2 is a virtual station.

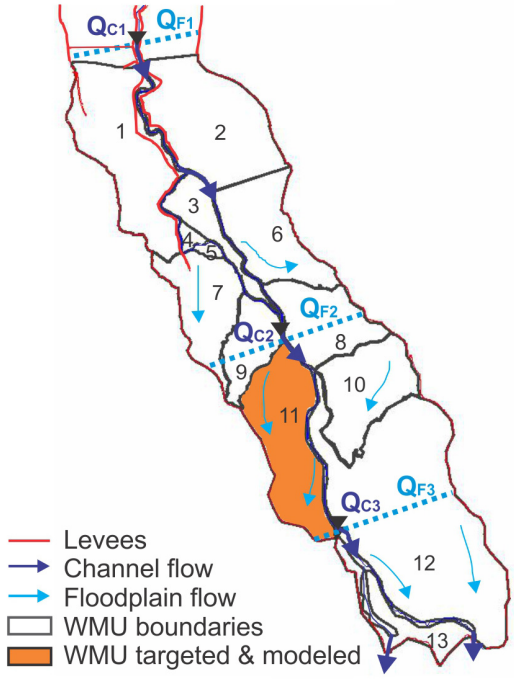

Figure 2. Schematic of local hydrodynamics in the ABFS including 13 water management units (WMUs): (1) Lake Henderson, (2) Alabama Bayou, (3) Werner, (4) Lost Lake, (5) Cow Island, (6) Bayou DeGlais, (7) Cocodrie Swamp, (8) Pigeon Bay, (9) Beau Bayou, (10) Flat Lake, (11) Buffalo Cove, (12) Upper Bell River, and (13) Six Mile Lake [*USACE*, 1982]. Black and light blue arrows are indicative of channel and floodplain flow directions. Light blue dotted lines represent floodplain flow boundary condition segments in the model. These lines are normal to the main channel direction between C2 and C3.

flow is represented using the diffusive approximation to the full 1-D St. Venant equations solved using a fully implicit Newton-Raphson scheme. Floodplain flows decoupled in x and y directions are implemented for a raster grid to give an approximation to a 2-D inertial wave. Mass conservation is simulated through the continuity equation (equation (1)). The LISFLOOD-ACC momentum equation includes the gravity and local acceleration terms from the shallow water equations but not the convective acceleration, and it is solved using an explicit finite difference scheme (equation (2)),

$$h_{i,j}^{t+\Delta t} = h_{i,j}^{t} + \Delta t \frac{Q_{xi,j-1}^{t} - Q_{xij}^{t} + Q_{yi,j-1}^{t} - Q_{yi,j}^{t}}{\Delta x^2}, \quad (1)$$

$$Q^{t} = \frac{q^{t} - g\, h_{\text{flow}}^{t} \Delta t \dfrac{\Delta (h^{t} + z)}{\Delta x}}{\left(1 + g\, h_{\text{flow}}^{t} \Delta t n^2 |q^{t-\Delta t}| / (h_{\text{flow}}^{t})^{10/3}\right)} \Delta x, \quad (2)$$

where h is the cell water depth, h_{flow} is the depth between cells through which water can flow, Q is the flow between cells, Δx is the cell size, n is Manning's roughness coefficient, q is Q from the previous time step divided by cell width, and g is gravity. Model implementation involves use of the diffusive solver for channel flow and equations (1) and (2) for 2-D inundation flow modeling, which has been parallelized using the shared memory Open Multi Processor (OpenMP) [*Neal et al.*, 2009] to reduce model run time.

[17] The Buffalo Cove model was run over a 62-d simulation period from 1 April 2008 to 1 June 2008 to accommodate at least two ALOS PALSAR acquisition dates on 16 April 2008 and 1 June 2008. Figures 3a and 3b illustrate that the simulation period comprises the high flow conditions associated with upper Mississippi River Basin snowmelt and spring rains, typical for this time of year.

[18] Model inputs included floodplain topography, bathymetric depths, channel widths, flow boundary conditions, and Manning's roughness coefficients for channels (n_C) and floodplains (n_F). The floodplain topography was constructed using a high-resolution 1 m LiDAR DEM of the basin [*U.S. Geological Survey (USGS)*, 2011]. The LiDAR survey was acquired in November 2010 during an optimal data collection window in terms of average river stage, average minimum temperature, and tree canopy. The vertical accuracy requirements meet or exceed the root-mean-square elevation (RMSE) of 18.5 cm required by National Standard for Spatial Data Accuracy (NSSDA). The 1 m LiDAR data was aggregated to 90 m to decrease grid resolutions and reduce model run time. The pixel-to-pixel noise is uncorrelated and reduces linearly in proportion to $1/\sqrt{n}$ as the data are aggregated, where n is the number of pixels being averaged [*Rodriguez et al.*, 2006]. The input LiDAR noise for model grids at 90 m is thus less than 0.2 cm.

[19] The averaging can result in a terrain data error due to the smoothing out of hydraulically relevant topography. This resolution has been shown in a number of previous studies to be appropriate to predict flood inundation in rural areas providing care is taken over the representation of linear features, such as embankments or levees, which can control the flow development [*Bates and De Roo*, 2000; *Horritt and Bates*, 2001]. Levees in the domain are narrow, typically less than 10 m wide and are sufficiently high so that floodwaters cannot overtop them for the chosen simulation period. In order to handle these subgrid-scale features [*Yu and Lane*, 2011], the levees in 1 m resolution were vectorized, extracted, and input into the 90 m resolution floodplain topography directly, without averaging out adjacent elevations that would have resulted in an uncharacteristically low height at 90 m resolution.

[20] Bathymetry was based on USACE hydrographic survey maps for the Atchafalaya [*USACE*, 2006] that provided bathymetric depth measurements every 10 feet along the river cross sections. Based on the bathymetry data set, the average bed elevations and channel widths were calculated as equivalent area rectangular cross sections at approximately every 1 km along the 34 km reach of the main channel in the Buffalo Cove region.

[21] To facilitate model set up, the model coordinates were rotated 15.67° clockwise north. The coordinate rotation makes the vertical axis in the model system parallel to the main channel direction and the horizontal axis to the floodplain flow condition. Figure 2 shows schematic local hydrodynamics in the study area. Flow pathways are well protected by high levees, thus water discharge per each

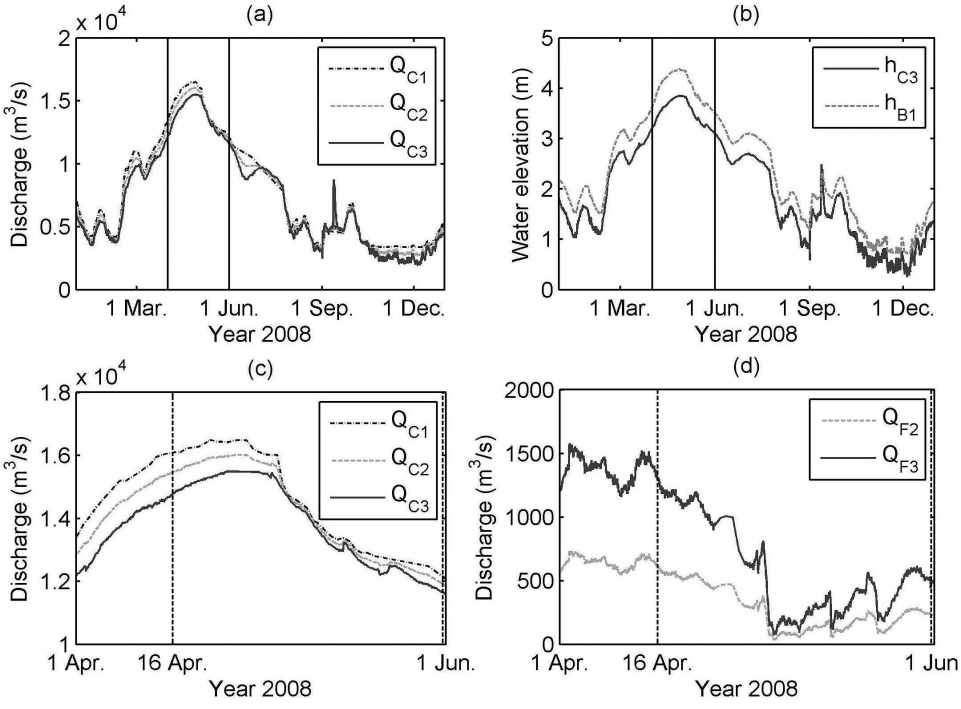

Figure 3. Daily time series of water discharges and elevations at gauges in the model area during 2008. (a, b) A l-y hydrograph including the model period during high water. The solid lines represent the first and last days of simulation on 1 April 2008 and 1 June 1 2008, respectively. Channel water elevations H_{C3} and H_{B1} are required for downstream channel boundary condition and calibration, respectively. Channel discharge Q_{C2} and floodplain discharge Q_{F2} are collected and calculated for upstream boundary condition. (c, d) Data fitted in the model period. The vertical dashed lines represent the ALOS PALSAR acquisition dates on 16 April 2008 and 1 June 2008. The detailed locations on C1, C2, C3, F2, and F3 are shown in Figure 2.

cross section along the main river channel is conservative. The continuity constraint is given by,

$$Q^t_{C1} + Q^t_{F1} = Q^t_{C2} + Q^t_{F2} = Q^t_{C3} + Q^t_{F3}, \tag{3}$$

where the superscript t represents time-varying discharge (Q), subscript digits are cross-section locations, and the subscript letters C and F represent the channel and floodplain, respectively. The channel flow from upstream to downstream results in more overbank flooding into the floodplain, thus the upstream channel discharge is greater than the downstream channel discharge (i.e., $Q^t_{C1} > Q^t_{C2} > Q^t_{C3}$). The upstream floodplain discharge is lower than the downstream floodplain discharge and floodplains around WMU1 and WMU2 are not flooded due to high levees which prevent overbank flow (i.e., $Q^t_{F3} > Q^t_{F2} > Q^t_{F1} = 0$).

[22] Boundary conditions for fluvial flooding applications normally require time-dependent discharge in the compound channel at the upstream end of the reach and the time-varying water elevation or gradient at the downstream end of the channel [*Bates et al.*, 2005]. Since there is no discharge station at the upstream boundary of the WMU1 domain, a virtual location C2 was created for which flow, Q^1_{C2}, was estimated using an inverse distance squared weighting (IDW) interpolation with channel discharges Q^1_{C1} at Krotz Springs and Q^1_{C3} at Myette Point [*Heijden and Haberlandt*, 2010]. The upstream channel boundary condition was thus calculated as,

$$Q^t_{C2} = f(Q^t_{C1}, Q^t_{C3})_{\mathrm{IDW}} = \frac{Q^t_{C1} \times d^t_{C2C3} + Q^t_{C3} \times d^2_{C1C2}}{d^2_{C1C2} + d^2_{C2C3}}, \tag{4}$$

where d_{ij} is the distance between locations of i and j.

[23] In addition to upstream channel discharge, upstream floodplain discharge was also set as a boundary condition. Although nonchannel flow at the boundary of the domain is usually negligible for fluvial flooding applications [*Bates et al.*, 2005], a time-dependent floodplain discharge was necessary since the upper domain boundary crosses the floodplain and substantial flow crosses into the domain during the 62-d simulation period. The upstream floodplain discharge derived from equations (3) and (4) (i.e., $Q^t_{F2} = Q^t_{C1} + Q^t_{F1} - Q^t_{C2}$; $Q^t_{F1} = 0$) was distributed equally among all of the upstream boundary grid cells.

[24] For the downstream condition, water elevation data at Myette Point (H^t_{C3}) were used. The other boundaries of the domain within the rectangular grid were set to a free flux condition to force the model to calculate the slope used for the normal depth calculation between the last two points. Figure 3 shows the daily time series of water elevations and discharges at gauge stations. Gauge stations are located at Krotz Springs (C1) and Myette Point (C3) along

the main channel and at Buffalo Cove (B1) in the bayous, whereas C2 is a virtual station. The gauge vertical datum were converted from the National Geodetic Vertical Datum of 1929 (NGVD29) into the National American Vertical Datum of 1988 (NAVD88) [*Milbert*, 1999] to fit the LiDAR floodplain elevations and bathymetry data set from USACE. In this study, the focus is on right (i.e., west) bank flooding in the Buffalo Cove WMU from the main channel of the Atchafalaya River.

[25] To calibrate the model response to Manning's roughness coefficients, a matrix of 36 simulations was run with values of n_C varying from 0.020 to 0.030 in steps of 0.002 in the channel, and n_F varying from 0.05 to 0.30 in steps of 0.05 in the floodplain. The range of values was chosen based on tables of typical n in various types of channels and floodplain [*Chow*, 1959]. Previous modeling in the Atchafalaya River Delta suggested that Manning's roughness coefficients in the area ranged from 0.01 to 0.06 for navigable waters, 0.01 to 0.02 for bayous, 0.03 to 0.06 for obstructed canals, and 0.2 to 0.5 for marsh and/or subaerial delta lobes [*Donnel et al.*, 1991; *Donnel and Letter*, 1992].

[26] The mean absolute error (MAE) and bias were used to evaluate the sensitivity of the model to the range of Manning's coefficients, or.

$$\mathrm{MAE} = \frac{1}{N}\Sigma_{i=1}^{N}|M_i - O_i|, \tag{5}$$

$$\mathrm{bias} = \frac{1}{N}\Sigma_{i=1}^{N}(M_i - O_i), \tag{6}$$

where M is the model and O is the observation (i.e., gauge height or interferometry height differences). The MAE and bias were computed for all points where there were observations and all were weighted equally. All of the model results for the total model period of 62 d are included in this calibration. Further details of both calibration approaches, using water elevations of gauge measurements and water elevation changes from SAR interferometry, are described in sections 5.1 and 5.2, respectively.

4.2. SAR Interferometry

[27] The Japan Aerospace Exploration Agency's (JAXA's) Advanced Land Observing Satellite (ALOS), a follow-on mission for the Japanese Earth Resources Satellite-l (JERS-l), carries the Phased Array type L-band Synthetic Aperture Radar (PALSAR). The PALSAR scenes are HH polarized and L-band (wavelength: 23.62 cm). The incidence angles of PALSAR scenes are ~38.7° from descending passes. The PALSAR swath of path 168 and frame 590 were collected on 16 April 2008 and 1 June 2008. As illustrated in Figure 1, the SAR image covers the central ABFS including the Buffalo Cove WMU.

[28] Measurements of water elevation changes in time (dh/dt) for the model domain were obtained from repeat-pass PALSAR interferometry and were used in the model calibration. SAR interferometric processing followed the two-pass method [*Massonnet et al.*, 1993]. The interferometric phase includes satellite orbit, topographic relief, and any changes in the radar range (i.e., floodplain water elevation change in this study). The orbit-related phase was subtracted through a flat earth phase removal that calculates satellite state vectors given by the system file and adjusts baseline errors based on the residual phase in the interferogram. As the most critical parameter in SAR interferometry, baseline is a measure of the distance between the two SAR antenna locations. The topographic-related phase was subtracted using the Shuttle Radar Topography Mission (SRTM) C-band elevation data to make the remaining differential phase dependent on floodplain water elevation changes. Interferometrically measured water elevation changes in the direction of the radar line-of-sight (LOS) were converted to a vertical displacement in terms of the wavelength and incidence angle of the PALSAR scenes [*Massonnet and Feigl*, 1998]. In this processed interferogram, 2 π radians of interferometric phase are equivalent to 15.1 cm of vertical height change.

[29] SAR interferometry with a short spatial baseline is more appropriate to provide water elevation changes and calibrate the corresponding model products as compared to a long baseline. Short perpendicular components in the baseline yield more topographic relief per phase cycle than long baselines, thus more reliable estimates of water elevation changes [*Zebker and Villasenor*, 1992]. In this study, the ALOS PALSAR L-band interferogram were processed with a perpendicular baseline of –219 m at the center of the satellite acquisition. The short baseline indicates that 2 π radians of phase are equivalent to ~204 m of topographic relief (i.e., the ambiguity height), whereas depending on the incidence angle, the same 2 π radians are also equivalent to ~15.1 cm of vertical water elevation change [*Massonnet and Feigl*, 1998]. The short perpendicular baselines and the C-band SRTM relative height errors of 5.5 m [*Farr et al.*, 2007] cause 0.17 radians of phase change, which are equivalent to 0.4 cm of vertical displacement. The accuracy of this displacement measurement is a function of the local coherence as well as of our ability to separate the topographic phase component from the total observed phase. The mean coherence of 0.35 in the modeled floodplain yields an expected phase noise value of less than 0.4 radian error for 21 looks used in the processing [*Zebker and Villasenor*, 1992; *Li and Goldstein*, 1990], which is equivalent to less than 1.0 cm of vertical displacement. The scale errors in the observed dh/dt are small enough to calibrate the modeled dh/dt and provide the optimum Manning's roughness.

[30] Figure 4 shows differential wrapped interferometric fringes in the floodplain. The patterns of a cycle of interferometric phase (i.e., fringe) imply that the basin consists of various independent hydrodynamic units as defined by the *USACE* [1982]. Distinct changes in the interferometric dh/dt measurements are located along the WMU boundaries. The Buffalo Cove and Upper Bell River WMUs show a clearer flow pattern of floodwater in the PALSAR interferometric phase as compared to any other WMUs. This provides more spatial variation in water elevation changes and is therefore a more rigorous test of the floodplain model performance. Most of the WMUs exhibit homogenous values in the interferogram. However, the Buffalo Cove and Upper Bell River WMUs show a sheet flow pattern and the Bayou DeGlais WMU shows a sharp distinction in the middle of the floodplain due to a navigable waterway. The differential phase wrapped in a cycle of 2 π radians is unwrapped with a minimum of cost flow

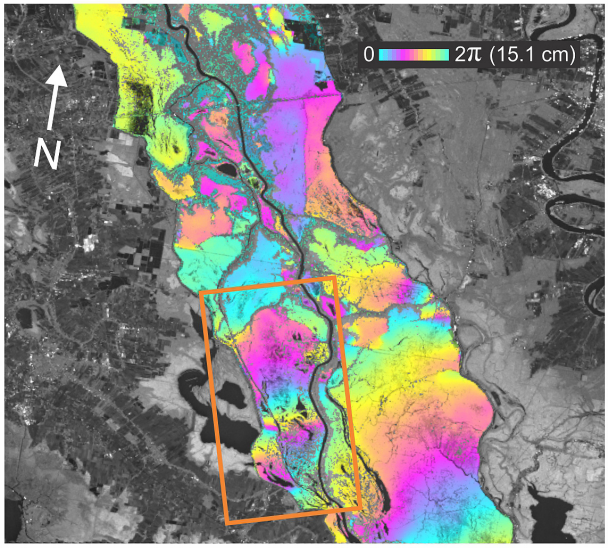

Figure 4. Differential wrapped interferogram of L-band PALSAR superimposed on the image reflectivity map in the ABFS. The orange rectangular box shows the location of the LISFLOOD model area. The color scale represents one cycle of interferometric phase that can be interpreted as 15.1 cm in vertical displacement. These fringes represent water elevation changes between 16 April 2008 and 1 June 2008.

techniques and a triangular irregular network to provide water elevation changes. In the phase unwrapping stage, adaptive radar interferogram filtering was applied to reduce noise and enhance fringe visibility. The unwrapped differential phase corresponds to relative water elevation changes. The interferometric SAR measurements require a reference datum to convert from the relative water elevation changes to absolute values [*Jung et al.*, 2010]. For this reference datum, gauge B1 was used, where the water level decreased 71 cm. (i.e., $dh/dt = -71$ cm over 46 d from 16 April 2008 to 1 June 2008; see h_{B1} in Figure 3b). The unwrapped and absolute interferometric measurements were used to calibrate the model water elevation changes.

5. Results

5.1. Calibration of Model Water Elevations (*h*) With Gauge Measurement

[31] LISFLOOD was first calibrated in terms of water elevations at the Buffalo Cove (B1) gauge using a matrix of 36 simulations with various Manning's roughness coefficients of the channel, n_C and the floodplain, n_F. For each simulation, the MAE was computed based on the daily water elevation differences between model and gauge measurement for the entire 62-d simulation period. The best-fit model of n_C and n_F was then determined as the lowest MAE in the three-dimensional space plot of MAE, n_C and n_F. Figure 5 shows the calibration surfaces for MAE and bias. The models with 0.022 to 0.026 in n_C and 0.10 to 0.20 in n_F show less than 10 cm in MAE. The optimum lies at 0.024 in n_C and 0.10 in n_F with 3.8 cm in MAE. The calibration surfaces show the L-shaped optimal region typical for 2-D hydraulic models optimized against single gauge or flood extent data [see, for example, *Fewtrell et al.*, 2011]. Here an increase in channel friction can be compensated for by a decrease in floodplain friction (and vice versa) to yield identical MAE or global goodness-of-fit for a range of channel and floodplain friction combinations. It can be seen that as one moves away from the optimal L-shaped region, MAE is greater with increasing gradient.

[32] The bias calibration surface shows that as n_C increases, bias increases and becomes less sensitive to n_F. It implies that modeling water elevations at gauge B1 in bayous is more dependent on the Manning's roughness coefficient of the main channel than that of the surrounding floodplain. The generally positive bias means that modeled water elevations are greater than the gauge measurement (see equation (6)). This agrees with the notion that as channel roughness

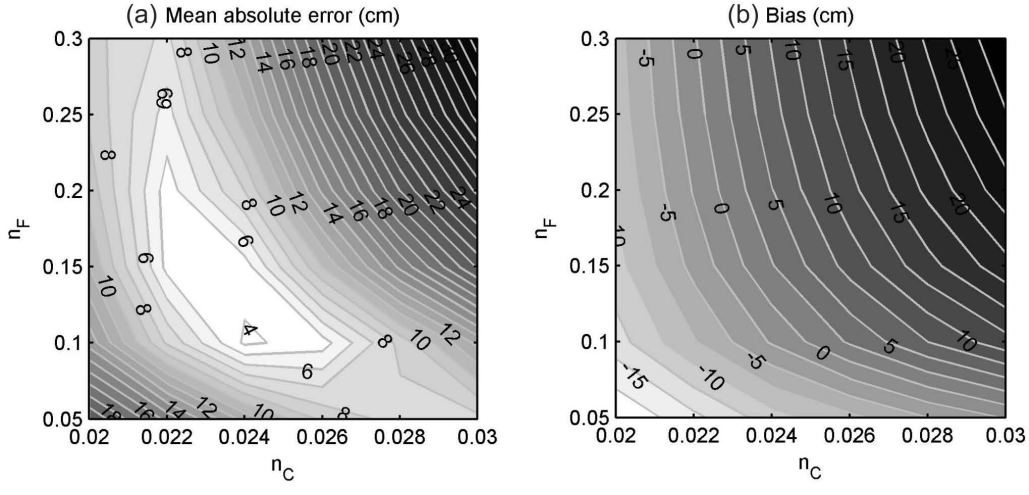

Figure 5. Calibration surfaces for (a) mean absolute error and (b) bias in terms of water elevations at gauge (B1) Buffalo Cove as function of channel (horizontal axis) and floodplain (vertical axis) Manning's roughness coefficients. The optimum roughness, determined as the lowest MAE equal to 3.8 cm, lies at 0.024 for channel n_c and 0. 10 for floodplain n_f.

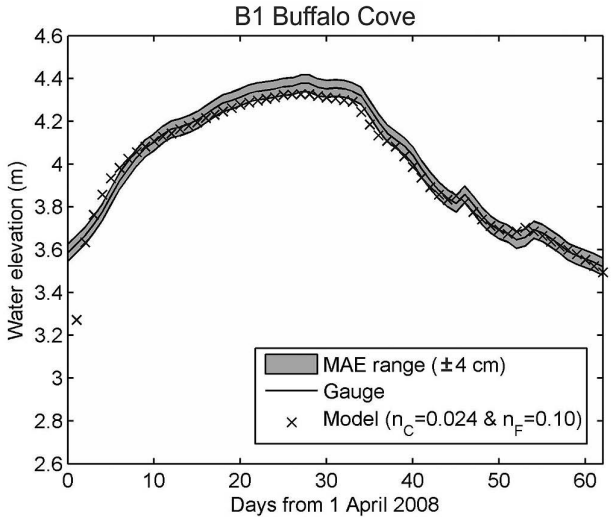

Figure 6. Model water elevations compared to actual water elevations at gauge (B1) Buffalo Cove. The model after 2 d in simulation starts to fit the gauge water elevations within ±4 cm in MAE with Manning's roughness coefficients of 0.024 in the channel and 0.10 in the floodplain.

increases, water elevation and storage must increase. Higher channel roughness decreases water velocity, thereby requiring a greater cross section to maintain the same outflow. The daily time series of water elevation in the best-fit model is shown in Figure 6. It reveals that after 2 d of initiating the simulation, the model reaches a stable stage and the model results fit the gauge water elevations within ±4 cm MAE. This is an excellent result given typical terrain and discharge errors, and within an engineering study would likely be used to indicate a model that could provide information in flood risk management decisions. In scientific terms, it is, however, a relatively limited test since the model performance is only evaluated at a single point with the domain.

5.2. Calibration of Model Water Elevation Changes (dh/dt) With SAR Interferometry

[33] The model is calibrated in terms of water elevation changes in the Buffalo Cove WMU using the same simulations as performed in section 5.1. However, instead of using one in situ gauge with a continuous height record, calibration is conducted using two images of height covering the entire flooded domain, separated by 46 d.

[34] The MAE is again used to find the best-fit model of n_C and n_F against water elevation changes calculated from ALOS PALSAR interferometry from 16 April 2008 to 1 June 2008. Figure 7 shows the calibration surfaces for MAE and bias. The models with 0.024 to 0.028 in n_C and 0.10 in n_F show a MAE of less than 8 cm over the 46-d period. The optimum lies at 0.028 in n_C and 0.10 in n_F with a MAE of 5.7 cm, which are similar but not identical to the Manning's roughness coefficients calibrated in section 5.1. The bias calibration surface shows that as n_F increases, bias decreases, being less sensitive to n_C. It implies that obtaining an optimal match between floodplain dh/dt measurements and the LISFLOOD-ACC model for the Buffalo Cove WMU is more dependent on the Manning's roughness coefficient of the floodplain compared to that of the main channel. The negative bias means that model water elevation change is actually less than that indicated by the interferometric measurements (see equation (6)). This is consistent with the notion that floodplain water elevations are less sensitive with higher roughness in the floodplain due to the lower floodplain velocities. Total frictional force (F) is proportional to Manning's roughness (n) and the square of flow velocity (v^2), so model sensitivity to friction is a nonlinear function of the flow velocity (v). When v is low, the modeled water levels become dramatically less sensitive to n.

[35] Figure 8 shows the water elevation change maps calculated from the best-fit model and SAR interferometry. The modeled dh/dt is calculated by subtracting the water elevation map on 16 April 2008 from that on 1 June 2008.

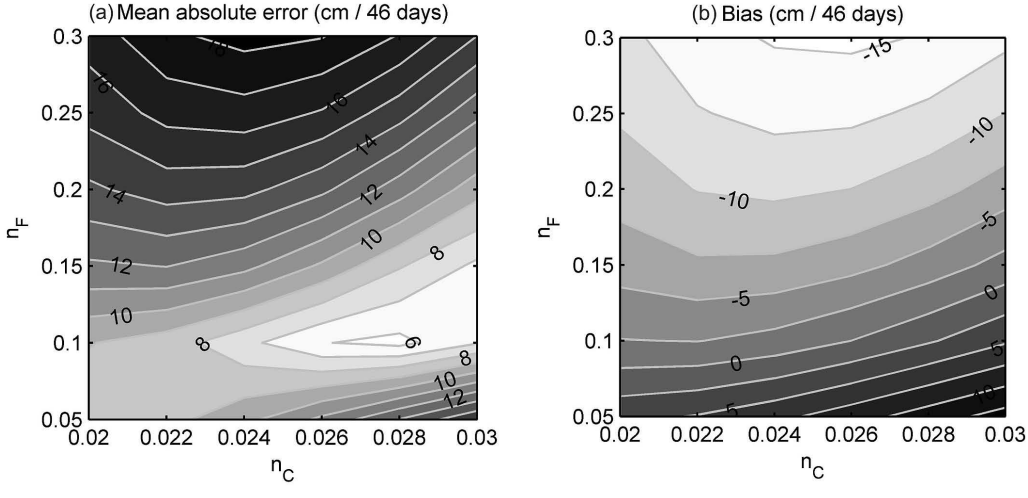

Figure 7. Calibration surfaces for (a) mean absolute error and (b) bias in terms of water elevation changes in the Buffalo Cove WMU as function of channel (horizontal axis) and floodplain (vertical axis) Manning's roughness coefficients (n). The optimum lies at 0.028 for channel n_c and 0.10 for floodplain n_f with 5.7 cm MAE for the 46-d simulation period.

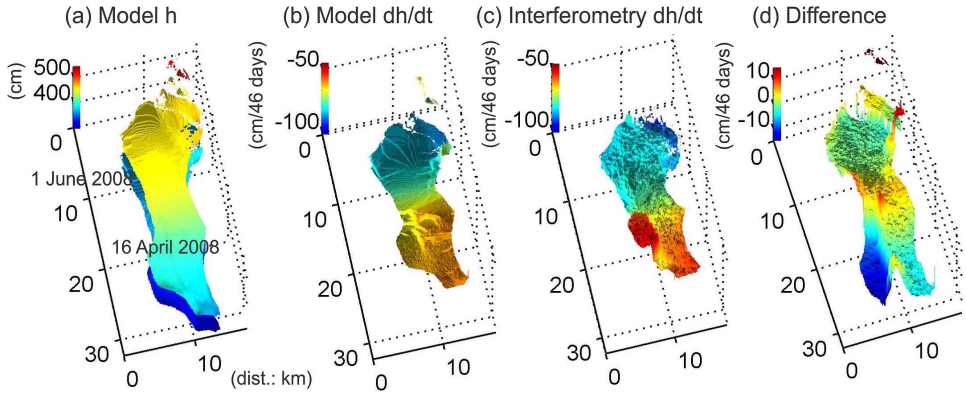

Figure 8. (a) Water elevation maps on 16 April 2008 (upper) and 1 June 2008 (lower). (b) Water elevation change map calculated from the calibrated model. (c) Water elevation change map from SAR interferometry. (d) Difference of water elevation change from between the (b) model and the (c) SAR interferometry.

The interferometrically measured dh/dt in Figure 8 are the absolute water elevation changes, which are referenced and unwrapped from the differential wrapped interferogram in Figure 4. The dh/dt in Buffalo Cove WMU ranges from –100 to –50 cm over 46 d showing that the floodplain is draining over the this period. The largest difference in dh/dt between model and SAR interferometry was exhibited in the southwest part of the WMU. It appears that inside waterways hold floodwater moving from east to west and add more complexity into the local floodplain dynamics than is captured by this model. The interferometry demonstrates that the southwest part exhibits a distinct difference in the spatial gradients of water elevation changes as compared to the surrounding area, which are microterrain effects that are not predicted by the model in a 90 m grid.

5.3. Estimation of Water Storage Changes (dS/dt) in Buffalo Cove WMU

[36] The daily modeled dS/dt is calculated by multiplying dh/dt by the grid cell area. The model dh/dt calibrated by SAR interferometry is used to calculate dS/dt,

$$dS^t/dt = S^t - S^{t-1} = \Sigma_{i=1}^{N}(h_i^t - h_i^{t-1}) \times dx \times dy, \qquad (7)$$

where t ranges from 1 to 62 as a simulation day and dx and dy are 90 m for a given grid box.

[37] The time series dS/dt is shown in Figure 9a for daily as well as 5- and 10-d moving averages to highlight longer-term trends. The daily storage changes in the model domain of ~230 km^2 range approximately from $+10^7$ m^3 d^{-1} to -10^7 m^3 d^{-1} during the modeled period. The water storage changes are positive at the beginning whereas they turn to be negative after 27 April 2008 with some variations.

[38] The relationship between the model water storage changes (dS/dt) and water elevation changes (dh/dt) at the Buffalo Cove gauge (B1), shown in Figure 9b, indicates a strong linear relationship, except for three outliers generated at the beginning of the simulation. It implies that the model requires more than 3 d to wet the whole floodplain and to provide reasonable values of water elevations in the floodplain of the WMU. The first polynomial regression model ($y = 2,216,650 \times x + 52,421$; $y : dS/dt$, $x : dh/dt$) exhibits an R^2 of 0.94. The residuals of the regression model suggest that dh/dt at the Buffalo Cove gauge cannot be representative of dh/dt across all of the Buffalo Cove WMU floodplain. As can be seen in Figure 8, the dh/dt varies markedly in space. Maps of h and dh/dt in Figure 10

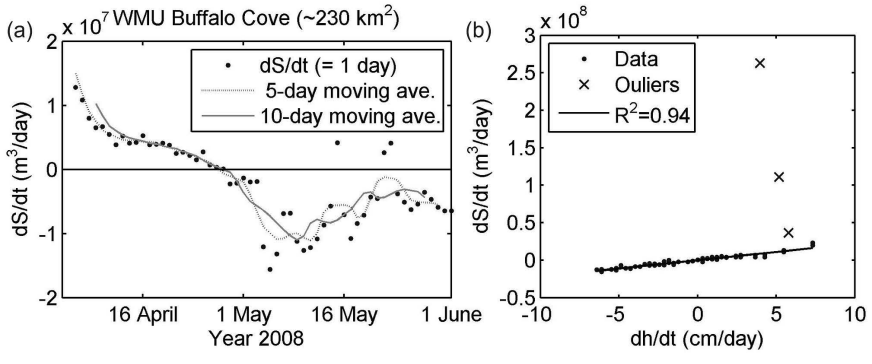

Figure 9. (a) Daily time series of water storage changes in the area of ~230 km^2 in the Buffalo Cove WMU. The 5 and 10 d moving averages are performed to demonstrate the trend of the water storage changes. (b) Relationship between model dS/dt in Buffalo Cove WMU and dh/dt at the (B1) Buffalo Cove gauge. The goodness of fit (R^2) is 0.94 based on the first polynomial regression model without three outliers that are generated before the model is stabilized.

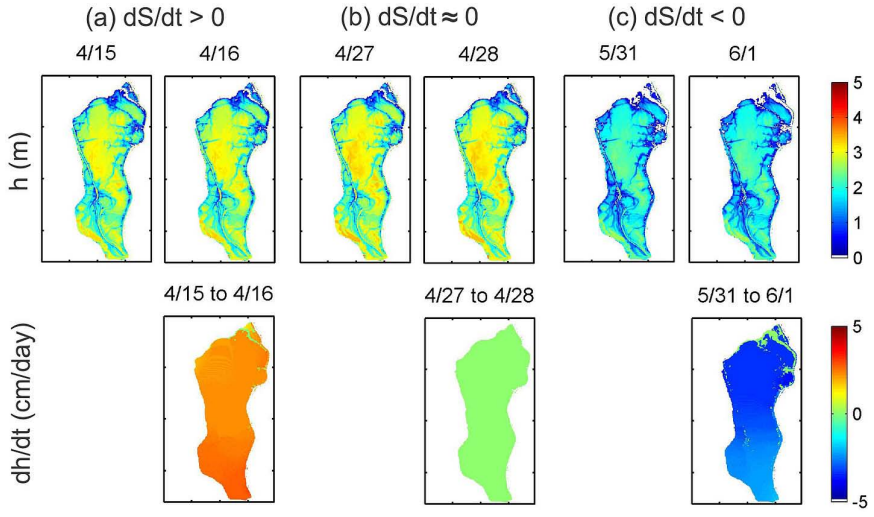

Figure 10. (Top row) Water depth maps relative to the LiDAR floodplain elevation and (bottom row) water depth change maps when *dS/dt* is (a) positive, (b) near zero, and (c) negative.

exhibit water storage changes that are positive, near zero, and negative. The maps of h show instances of floodplain filling and emptying. For instance, the average dh/dt of the WMU between 15 April 2008 and 16 April 2008 is 2.4 cm d^{-1} when the corresponding dS/dt is 5.5×10^6 m^3 d^{-1}. On the contrary, the dh/dt average of the WMU between 31 May 2008 and 1 June 2008 is –2.9 cm d^{-1} when the corresponding dS/dt is -6.6×10^6 m^3 d^{-1}. The dh/dt maps in the lower panel of Figure 10 show less variation within the WMU as compared to the dh/dt maps shown in Figure 8 because the time interval (dt) is 1 d shorter than 46 d in Figure 8.

6. Discussion of Sensitivity to Different Errors

[39] Two approaches to calibrate a 2-D hydrodynamic model were investigated, one using a single in situ gauge measurement and the second using SAR interferometry. Each approach calibrates the model in terms of different model products that have different space (i.e., dimensionality) and timescales. The first calibration uses time series of water elevations at one specified gauge station for the total simulation period of 62 d. Because of the gauge location in the bayou, the calibration shows more dependency on channel roughness relative to floodplain roughness.

[40] The second calibration uses water elevation changes calculated from SAR interferometry across the whole WMU area for one time interval of 46 d between two successive overpasses of the PALSAR satellite. This is a particularly stern test for a 2-D hydrodynamic model because the calibration requires accurate prediction of spatial patterns of water elevation change over a long simulation period. Since SAR interferometry receives strong scatters in the floodplain due to the double-bounce effect as compared to specular scattering of open water [*Lu and Kwoun*, 2008; *Jung and Alsdorf*, 2010], this calibration shows more dependency on floodplain roughness.

[41] Most 2-D floodplain modeling requires a longer spin-up time, as compared to l-D channel modeling, in order to wet the floodplain as well as channel for stabilization of the floodplain dynamic in the model. The spin-up time in the calibration with SAR interferometry requires at least 3 d more than the 2 d required with only gauge measurements. The different calibration methods suggest the same floodplain roughness, but different channel roughness in their best-fit models, which can be explained by different model products used in their calibrations. The pattern and trend of the MAE and bias calibration surfaces imply that calibration against different data sets would lead a user to make different conclusions regarding the model's differential sensitivity to channel and floodplain friction. Practically, the real meaning of roughness as an effective parameter is a component of topography that has to be calculated to optimize the agreement between model predictions and measurements [*Lane*, 2005]. The calibrated roughness can be a valuable reference to the hydrodynamic modeling community as it is properly adjusted along water stage, grid resolution, and model feature.

[42] The sensitivity to upstream discharge was investigated by changing the flow by ±20% in increments of 5%, for both calibration approaches. Root-mean-square deviation (RMSD) in the modeled h and dh/dt was computed for each flow, averaged across the domain, using the best-fit model of 0.028 in n_C and 0.10 in n_F. Assuming that even for good gauges, Q error is likely to be ±10% [*Di Baldassarre and Montanari*, 2009], Figure 11 indicates that this likely error in upstream Q leads to ~10 cm of errors in the modeled h maps on both 16 April 2008 and 1 June 2008 and less than 2.5 cm in the modeled dh/dt map (Figure 11). This implies that the effect of an error in Q on the absolute water elevations is much larger than the effect of the same Q error on the water elevation changes. The deviation on absolute water elevations can be compensated for in any modeling study with a uniform offset derived from a contemporaneous ground truth campaign. The deviation of 2.5 cm in the modeled dh/dt can be regarded as the range of acceptable differences between the observed dh/dt and the modeled one. It suggests that within the $Q \pm 10\%$ error ranges, 54% of dh/dt map in Figure 8d shows a good agreement between the model and the interferometric measurement. The slight difference in channel roughness between two calibration methods (i.e.,

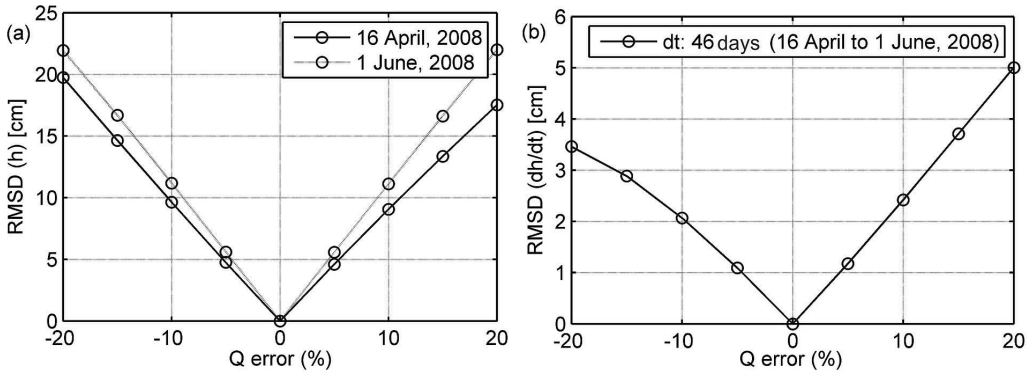

Figure 11. Results of the modeled h and dh/dt to uncertainty in upstream Qs, varying from –20% and 20% in steps of 5%. The calibrated model of 0.028 in n_C and 0.10 in n_F is used as a behavioral model. The h maps on 16 April 2008 and 1 June 2008 and dh/dt map for the 46 d are shown in Figures 8a and 8b.

0.024/0.1 and 0.028/0.1 in n_C/n_F, respectively) leads to ~1.5 cm of the modeled dh/dt difference in Figure 7a and this can be also explained within the $Q \pm 10\%$ error ranges.

[43] In both gauge stage h and interferometric SAR dh/dt calibrations, the tolerable difference between model and data is much smaller as some of key errors drop out. Error sources in the LiDAR data, a terrain data error resulting from the averaging to 90 m, the observed h data, and the measured dh/dt are less than 1 cm, whereas the likely $\pm 10\%$ errors in Q result in less than 2.5 cm in the modeled dh/dt. It is noted that these errors are not necessarily additive and not all will be at a maximum at the same time.

[44] The Buffalo Cove WMU as a model domain is mostly covered with woody wetland, yet the Atchafalaya River Basin includes various land covers of urban, pasture, cultivated crops, woody wetlands, and emergent herbaceous wetlands in the 2006 National Land Cover Data (NLCD) [*Fry et al.*, 2011]. For large floodplain modeling, the roughness can be assigned in more detail based on land use and land cover [*Kalyanapu et al.*, 2009]. To take advantage of land cover data to improve the roughness assignment, optimization algorithms need to be utilized for multiparameter calibration [*Zhang et al.*, 2008].

7. Conclusions

[45] The 2-D LISFLOOD-ACC model was applied to spring flooding in the central ABFS and calibrated using two independent approaches. A traditional approach used a continuous temporal record of in situ, point water-level gauge measurements. The second new approach, employed temporal (dh/dt) and spatial (dh/dx, dh/dy) variations of water levels derived from ALOS PALSAR interferometry, observed at two separate times. Although the two different approaches yielded slightly different values for channel Manning's n, the favorable comparison in results establishes the feasibility of a satellite-based approach, at least for these particular basin and flow conditions. Results were facilitated by a relatively simple spring hydrograph with few spikes in river discharge, and well-defined floodplain boundaries. Overall, the results offer a new approach for satellite-based calibration of hydrodynamic models, especially in regions of sparse in situ data.

[46] The slight difference in calibration results are to be expected given that the two independent approaches relied on two different data sets, in one case a continuous time series of channel elevations at a single point, and in the second, a continuous spatial distribution of water levels and slopes at two points in time. However, differences also might be due to artifacts in the observed data, or microterrain effects that are not picked up in a 90 m grid, or error-associated with assumptions in the hydraulic model. Results indicate that even a few observations can quantify the floodplain water elevation and reveal the complexity of the floodplain hydrodynamics. This study highlights the importance and potential advantage of 2-D interferometric SAR techniques to support 2-D floodplain model calibration.

[47] Second, results on the spatial and temporal variations of water elevations $\left(\frac{dh/dt}{dx}, \frac{dh/dt}{dy}\right)$ are demonstrated to be useful to estimate daily time series of water storage changes (dS/dt) in the Buffalo Cove WMU. Since the model is validated in terms of dh/dt from SAR interferometry, the improved model can generate reliable estimates of dS/dt and the moving averages can be useful to see the trend of basinwide water storage changes.

[48] Last, the results indicate the feasibility of using SAR interferometry for enhanced prediction and assessment capabilities for future flood events in the floodplain. The hydrodynamic modeling calibrated by SAR interferometry can be extended into higher grid resolution and/or larger domains to study the floodplain hydrodynamics in more detail. For the purpose of future flood control and risk management, modeling could focus on monitoring the basin in near real time with the help of parallel computation using multicore processors.

[49] **Acknowledgments.** This research was supported by an appointment to the NASA Postdoctoral Program (NPP) at the Goddard Space Flight Center (GSFC), administered by Oak Ridge Associated Universities (ORAU) through a contract with NASA. We acknowledge the NASA Center for Climate Simulation (NCCS) and the OH Supercomputer Center (OSC) for use of the computing resources. The Ohio State University (OSU) component of the research is partially supported by NASA's Hydrology Program and OSU's Climate, Water and Carbon Program. We thank Yvonne Allen in USACE for sharing her knowledge of the Atchafalaya Basin Floodway System. LiDAR data were undertaken and provided by U. S. G. S. National Geospatial Program and U. S. G. S. Coastal and Marine Geology Program. ALOS PALSAR data were provided by AK Satellite Facility (ASF).

References

Allen, Y. C., G. C. Constant, and B. R. Couvillion (2008), Preliminary classification of water areas within the Atchafalaya Basin floodway system by using Landsat imagery, *U.S. Geol. Surv., Open-File Rep., 2008-1320*.

Alsdorf, D., P. Bates, J. Melack, M. Wilson, and T. Dunne (2007), Spatial and temporal complexity of the Amazon flood measured from space, *Geophys. Res. Lett.*, *34*, L08402, doi:10.1029/2007GL029447.

Alsdorf, D. E. (2003), Water storage of the central Amazon floodplain measured with GIS and remote sensing imagery, *Ann. Assoc. Amer. Geographers*, *93*, 55–66.

Alsdorf, D. E., J. M. Melack, T. Dunne, L. A. K. Mertes, L. L. Hess, and L. C. Smith (2000), Interferometric radar measurements of water level changes on the Amazon floodplain, *Nature*, *404*, 174–177.

Alsdorf, D. E., T. Dunne, J. M. Melack, L. C. Smith, and L. L. Hess (2005), Diffusion modeling of recessional flow on central Amazonian floodplains, *Geophys. Res. Lett.*, *32*, L21405, doi:10.1029/2005GL024412.

Bates, P. D., and A. P. J. De Roo (2000), A simple raster-based model for floodplain inundation, *J. Hydrol.*, *236*, 54–77.

Bates, P. D., M. G. Anderson, L. Baird, D. E. Walling, and D. Simm (1992), Modelling floodplain flow with a two-dimensional finite element scheme, *Earth Surf. Processes Landforms*, *17*, 575–588.

Bates, P. D., R. J. Dawson, J. W. Hall, M. S. Horritt, R. J. Nicholls, J. Wicks, and M. A. A. M. Hassan (2005), Simplified two-dimensional numerical modelling of coastal flooding and example applications, *Coast. Eng.*, *52*, 793–810.

Bates, P. D., M. S. Horritt, and T. J. Fewtrell (2010), A simple inertial formulation of the shallow water equations for efficient two-dimensional flood inundation modelling, *J. Hydrol.*, *387*, 33–45.

Bradbrook, K. F., S. N. Lane, S. G. Waller, and P. D. Bates (2004), Two-dimensional diffusion wave modelling of flood inundation using a simplified channel representation, *Int. J. River Basin Manage.*, *3*, 211–223.

Chow, V. T. (1959), *Open Channel Hydraulics*, 483 pp., McGraw-Hill, N. Y.

Couvillion, B. R., J. A. Barras, G. D. Steyer, W. Sleavin, M. Fischer, H. Beck, N. Trahan, B. Griffin, and D. Heckman (2011), Land area change in coastal Louisiana from 1932 to 2010, *U.S. Geol. Surv. Scientific Investigations Map 3164*, scale 1:265,000, 12 pp.t

DHI Water and Environment (2001), *MIKE11 Hydrodynamic Reference Manual*, 516 pp., DHI Software, Horshølm, Denmark.

Di Baldassarre, G., and A. Montanari (2009), Uncertainty in river discharge observations: A quantitative analysis, *Hydrol. Earth Syst. Sci. Discuss.*, *6*, 39–61.

Di Baldassarre, G., G. Schumann, and P. D. Bates (2009), A technique for the calibration of hydraulic models using uncertain satellite observations of flood extent, *J. Hydrol.*, *367*, 276–282.

Donnell, B. P., and J. V. Letter (1992), The Atchafalaya River Delta Rep. 12: Two-dimensional modeling of alternative plans and impacts on the Atchafalaya bay and Terrebonne marshes, *Rep. AD-A246-089*, U.S. Army Engineer District, New Orleans, La.

Donnell, B. P., J. V. Letter, and A. M. Tetter (1991), The Atchafalaya River Delta Rep. 11: Two-dimensional modeling, *Rep. AD-A237-369*, U.S. Army Engineer District, New Orleans, La.

Ervine, D. A., and A. B. MacCleod (1999), Modelling a river channel with distant floodbanks, *Proc. Inst. Civil Eng.*, *136*, 21–33.

Falconer, R. A. (1986), A water quality simulation study of a natural harbor, American Society of Civil Engineers, *J. Waterw. Port Coast. Ocean Eng.*, *112*, 1, 15–34.

Farr, T. G., et al. (2007), The Shuttle Radar Topography Mission, *Rev. Geophys.*, *45*, RG2004, doi:10.1029/2005RG000183.

Fewtrell, T. J., J. C. Neal, P. D. Bates, and P. J. Harrison (2011), Geometric and structural model complexity and the prediction of urban inundation, *Hydrol. Processes*, *25*, 3173–3186.

Fread, D. L. (1985), Channel routing, in *Hydrological* Forecasting, edited by M. G. Anderson and P. Burt, chapt. 14, pp. 437–503, John Wiley, Chichester, U. K.

Fry, J., G. Xian, S. Jin, J. Dewitz, C. Homer, L. Yang, C. Barnes, N. Herold, and J. Wickham (2011), Completion of the 2006 National Land Cover Database for the Conterminous United States, *Photogramm. Eng. Remote Sens.*, *77*, 858–864.

Heijden, S., and U. Haberlandt (2010), Influence of spatial interpolation methods for climate variables on the simulation of discharge and nitrate fate with SWAT, *Adv. Geosci.*, *27*, 91–98.

Hess, L. L., J. M. Melack, S. Filoso, and Y. Wang (1995), Delineation of inundated area and vegetation along the Amazon floodplain with the SIR-C synthetic aperture radar, *IEEE Trans. Geosci. Remote Sens.*, *33*, 896–904.

Horritt, M. S., and P. D. Bates (2001), Effects of spatial resolution on a raster based model of flood flow, *J. Hydrol.*, *253*, 239–249.

Hunter, N. M., et al. (2008), Benchmarking 2D hydraulic models for urban flooding, *Proc. Inst. Civil. Eng.*, *16*, 13–30.

ISIS FLOW (2001), *User manual*, vol. 1, Halcrow/HR Wallingford, Oxfordshire, U. K. [available at http://www.halcrow.com/isis/isisfree.asp].

Jung, H. C., and D. Alsdorf (2010), Repeat-pass multi-temporal interferometric SAR coherence variations with Amazon floodplain and lake habitats, *Int. J. Remote Sens.*, *31*, 881–901.

Jung, H. C., J. Hamski, M. Durand, D. Alsdorf, F. Hossain, H. Lee, A. K. M. A. Hossain, K. Hasan, A. S. Khan, and A. K. M. Z. Hoque (2010), Characterization of complex fluvial systems via remote sensing of spatial and temporal water level variations, *Earth Surf. Processes Landforms*, *35*, 294–304.

Kalyanapu, A., S. J. Burian, and T. N. McPherson (2009), Effect of land use-based surface roughness on hydrologic model output, *J. Spat. Hydrol.*, *9*, 51–71.

Kim, J., Z. Lu, H. Lee, C. K. Shum, C. M. Swarzenski, T. W. Doyle, and S. Baek (2009), Integrated analysis of PALSAR/Radarsat-l InSAR and ENVISAT altimeter data for mapping of absolute water level changes in Louisiana wetlands, *Remote Sens. Environ.*, *113*, 2356–2365.

Knabb, R. D., J. R. Rhome, and D. P. Brown (2006), *Tropical cyclone report: Hurricane Katrina: 23–30 August* 2005, National Hurricane Center, Miami, Fla., 42 pp.

Knabb, R. D., D. P. Brown, and J. R. Rhome (2007), *Hurricane Rita*, (available at http://www.nhc.noaa.gov/pdf/TCR-AL182005_Rita.pdf), National Hurricane Center, Miami, Fla.

Lake Pontchartrain Basin Foundation (LPBF) (2008), *Comprehensive recommendations supporting the use of the multiple lines of defense strategy to sustain coastal Louisiana, rep., version 1*, pp. 9–77, Lake Pontchartrain Basin Foundation, Metairie, La. [available at http://www.mlods.org/2008reportversion1.html].

Lake Pontchartrain Basin Foundation (LPBF) (2010), *Hydrology and hydrodynamic modeling of the Mississippi River in southeast Louisiana, rep., part I*, pp. 1–10, Lake Pontchartrain Basin Foundation, Metairie, La.

Lane, S. N. (2005), Roughness—time for a re-evaluation?, *Earth Surf. Processes Landforms*, *30*, 251–253.

Lee, H., C. K. Shum, Y. Yi, M. Ibaraki, J. Kim, A. Braun, C. Kuo, and Z. Lu (2009), Louisiana wetland water level monitoring using retracked TOPEX/POSEIDON altimetry, *Mar. Geod.*, *32*, 284–302.

Li, F. K., and R. M. Goldstein (1990), Studies of multibaseline spaceborne interferometric synthetic aperture radars, *IEEE Trans. Geosci. Remote Sens.*, *28*, 88–97.

Louisiana Department of Natural Resources (LDNR) (2010), *Atchafalaya Basin: FY 2010 annual plan*, pp. 3–5, Atchafalaya Basin Program, Louisiana Department of Natural Resources, Baton Rouge, La.

Lu, Z., and O. Kwoun (2008), Radarsat-l and ERS InSAR analysis over southeastern coastal Louisiana: Implications for mapping water-level changes beneath swamp forests, *IEEE Trans. Geosci. Remote Sens.*, *46*, 2167–2184.

Lu, Z., M. Crane, O. Kwoun, C. Wells, C. Swarzenski, and R. Rykhus (2005), C-band radar observes water level change in swamp forests. *EOS*, *86*, 141–144.

Lu, Z., J. Kim, H. Lee, C. Shum, J. Duan, M. Ibaraki, O. Akyilmaz, and C. Read (2009), Helmand River hydrologic studies using ALOS PALSAR InSAR and ENVISAT altimetry, *Mar. Geod.*, *32*, 320–333.

Massonnet, D., and K. L. Feigl (1998), Radar interferometry and its application to changes in the Earth's surface, *Rev. Geophys.*, *36*, 441–500.

Massonnet, D., M. Rossi, C. Carmona, F. Adragna, G. Peltzer, K. Feigl, and T. Rabaute (1993), The displacement field of the Landers earthquake mapped by radar interferometry, *Nature*, *364*, 138–142.

Meade, R. H. (1995), Contaminants in the Mississippi River 1987-92, *U.S. Geol. Surv. Circ.*, 1133, U.S. Geological Survey, Reston, Va.

Milbert, D. G. (1999), National Geodetic Survey (NGS) height conversion methodology, [available at http://www.ngs.noaa.gov/TOOLS/Vertcon/vert_method.html], National Geodetic Survey, NOAA, Silver Spring, MD.

Neal, J., G. Schumann, T. Fewtrell, M. Budimir, P. Bates, and D. Mason (2011), Evaluating a new LISFLOOD-FP formulation with data from the summer 2007 floods in Twekesbury, UK, *J. Flood Risk Manag.*, *4*, 88–95.

Neal, J. C., T. J. Fewtrell, and M. A. Trigg (2009), Parallelisation of storage cell flood models using OpenMP, *Environ. Modell. Software*, *24*, 872–877.

Rodriguez, E., C. S. Morris, and J. E. Belz (2006), A global assessment of the SRTM performance, *Photogramm. Eng. Remote Sens.*, *72*, 249–260.

Samuels, P. G. (1990), Cross section location in one-dimensional model, in *International Conference on River Flood Hydraulics*, edited by W. R. White, pp. 339–350, John Wiley, Chichester, U. K.

Samuels, P. G., and M. P. Gray (1982), *The FLUCOMP River Model Package: An Engineers Guide*, Rep. EX 999 Series, HR Wallingford, U. K.

Smith, L. C. (1997), Satellite remote sensing of river inundation area, stage, and discharge: A review, *Hydrol. Processes*, *11*, 1427–1439.

Syme, W. J. (1991), Dynamically linked two-dimensional/one-dimensional hydrodynamic modelling program for rivers, estuaries and coastal water, M.Eng.Sc. thesis, Univ. of Queensland, Aust.

U.S. Army Corps of Engineers (USACE) (1982), Atchafalaya Basin floodway system feasibility study, main rep. and final environmental impact statement, New Orleans District, La.

U.S. Army Corps of Engineers (USACE) (2001), *HEC-RAS River Analysis System, Hydraulic Ref. Manual*, version 3.0, Hydrologic Engineering Center, Davis, Calif.

U.S. Army Corps of Engineers (USACE) (2006), *Atchafalaya River System Hydrographic Survey Book*, New Orleans District, La, 136 pp.

U.S. Army Corps of Engineers (USACE) (2011), Morganza floodway, [available at http://www.mvn.usace.army.mil/bcarre/morganza.asp], USACE, New Orleans, La.

U.S. Environmental Protection Agency (USEPA) (1987), Saving Louisiana's coastal wetlands: The need for a long-term plan of action, report of the Louisianan wetland protection panel, *Rep. EPA-230-02-87-026*, pp. 3–28, Louisiana Geological Survey, US Environmental Protection Agency, Washington, DC.

U.S. Geological Survey (USGS) (2011), 2010 LiDAR elevation map for the Atchafalaya basin, [available at http://abp.cr.usgs.gov/Library/Default.aspx?keyword=Lidar], Louisiana Department of Natural Resources, Atchafalaya Basin Program's Natural Resource Inventory & Assessment System (NRIAS), Baton Rouge, La.

Vaughn, D. M., D. Rickman, and H. Oscar (1996), Modeling spatial and volumetric changes in the Atchafalaya Delta, Louisiana, *Geocarto Int.*, *11*, 71–80.

Villanueva, I., and N. G. Wright (2006), Linking Riemann and storage cell models for flood prediction, *Proc. Inst. Civil. Eng.*, *159*, *1*, 27–33.

Wang, F. C., V. Ransibrahmanakul, K. L. Tuen, M. L. Wang, and F. Zhang (1995), Hydrodynamics of a tidal inlet in Fourleague Bay/Atchafalaya Bay, Louisiana, *J. Coastal Res.*, *11*, 733–743.

Wilson, M., P. Bates, D. Alsdorf, B. Forsberg, M. Horritt, J. Melack, F. Frappart, and J. Famiglietti (2007), Modeling large-scale inundation of Amazonian seasonally flooded wetlands, *Geophys. Res. Lett.*, *34*, L15404, doi:10.1029/2007GL030156.

Yu, D., and S. N. Lane (2011), Interactions between subgrid-scale resolution, feature representation and grid-scale resolution in flood inundation modelling, *Hydrol. Processes*, *25*, 36–53.

Zanobetti, D., H. Longeré, A. Preissmann, and J. A. Cunge (1970), Mekong delta mathematical model program construction, *Proc. Amer. Soc. Civil Eng.*, *96*, 181–199.

Zebker, H. A., and J. Villasenor (1992), Decorrelation in interferometric radar echoes, *IEEE Trans. Geosci. Remote Sens.*, *30*, 950–959.

Zhang, X., R. Srinivasan, K. Zhao, and M. V. Liew (2008), Evaluation of global optimization algorithms for parameter calibration of a computationally intensive hydrologic model, *Hydrol. Processes*, *23*, 430–441.